



# Design and evaluation of surface functionalized superparamagneto-plasmonic nanoparticles for cancer therapeutics



M. Ravichandran<sup>a,1</sup>, Goldie Oza<sup>b,1</sup>, S. Velumani<sup>a,c,\*</sup>, Jose Tapia Ramirez<sup>b,\*\*</sup>, A. Vera<sup>d</sup>, L. Leija<sup>d</sup>

<sup>a</sup> Program on Nanoscience and Nanotechnology, Mexico

<sup>b</sup> Department of Genetics and Molecular Biology, Mexico

<sup>c</sup> Department of Electrical Engineering, Mexico

<sup>d</sup> Department of Electrical Engineering – Bioelectronics Section, CINVESTAV-IPN, Av. 2508 National Polytechnic Institute, Gustavo A. Madero, San Pedro Zacatenco, 07360 Mexico City, Mexico

## ARTICLE INFO

### Article history:

Received 9 February 2017

Received in revised form 18 March 2017

Accepted 26 March 2017

Available online 28 March 2017

### Keywords:

Multifunctional

Core-shell

Biocompatible

Drug kinetics

Hyperthermia

## ABSTRACT

Designing a multifunctional nanomaterial is always considered as a biggest concern in the field of nanomedicine which aims to promote versatile action in a single use from tracking to therapeutics. Therefore, metallic nanoparticles are well exploited as a major platform with the assemblage of surface modifications which can be effectively engaged for plenty of applications. Here, in this work, we have successfully amalgamated gold coated magnetite core-shell nanoparticles along with bio-functionalization of folic acid and doxorubicin to explore its possibility as a distinct nanocargo for cancer nanotheranostics. This unique combination of both magnetic and optical properties makes its function to be more precise. For example, in case of *in-vitro* drug-release studies more than 75% of drug moieties are released at acidic pH 5.4 and exactly fitting in first order rate kinetics. As gold shell retains the superparamagnetic nature of the core it exhibited high  $r_2$  values, and because of large relaxivities ( $r_2/r_1$ ) ratio, they are confirmed as  $T_2$ -weighted contrast agent by MRI. Finally, under microwave of 2.45 GHz exhibited enough heat which can induce both apoptosis & necrosis leading to cell death. Thus, we conclude that our nanoparticle can be a multitool for diagnosis and therapeutics for various human diseases.

© 2017 Elsevier B.V. All rights reserved.

## 1. Introduction

Cancer, considered as a hallmark of diseases which is responsible for second most mortality and morbidity rates. The greatest discovery in the fundamental cancer biology has not been transformed into clinical therapeutics. There is a vast incongruity existing due to lack of translational medicine targeting towards the cancerous cells both temporally and spatially. Moreover, the drugs available possess a plethora of side-effects and are incapable of circumventing the biophysical barriers posed by tumor

microphysiology. The two nano-vectors viz., drug-delivery and imaging have come to the rescue in such a debilitating condition of cancer therapeutics.

The recent upsurge of interest in medical nanotechnology has significantly expanded the breadth and depth of magnetic nanoparticle (MNPs) research. MNPs are exploited for various applications in biomedicine, such as Magnetic Resonance Imaging (MRI), drug-delivery and hyperthermia (Angelakeris, 2017; Licciardi et al., 2013; Reddy et al., 2012). But the biggest flaw in using MNPs is that they are highly reactive in nature, and moreover, they have the tendency to transform their oxidation states drastically. To circumvent this problem, there was a need of coating such particles with an inert transition metal i.e. gold (GNPs). This coating leads to stabilization of the particles, thus enhancing the biocompatibility as well as biodistribution in physiological conditions. Such a design of nanoparticles comprising of SPIONIC core and gold shell can perform multi-functions concomitantly

\* Corresponding author at: Program on Nanoscience and Nanotechnology, Mexico.

\*\* Corresponding author.

E-mail addresses: [velu@cinvestav.mx](mailto:velu@cinvestav.mx) (S. Velumani), [jtapia@cinvestav.mx](mailto:jtapia@cinvestav.mx) (J.T. Ramirez).

<sup>1</sup> Authors contributed equally to this work.

such as imaging, drug-delivery and hyperthermia. Such a nano-medicinal model containing **MNPs** can perform two functions:

- a enhance proton relaxation of specific tissues,
- b serve as MR imaging contrast agents.

The nanoshell made up of **GNPs** is surface plasmon resonance (SPR) active substance, which can interact with a linker and then orchestrate anti-cancer drugs (Alexiou et al., 2000; Cheng et al., 2005; Habib et al., 2008; Hergt and Dutz, 2007; Lübbe et al., 1996; Wilhelm et al., 2008).

Such a targeted drug delivery cargo can be accrued within the tumor site by different mechanisms such as externally applied magnetic field (Widder et al., 1978), enhanced permeation and retention of small nanoparticles (NPs) due to the leaky vasculature (Maeda et al., 2000) and folate receptor-based temporal and synaphic targeting. Once collated at the tumor site, such nanoflittas are incorporated *via* receptor-mediated endocytosis and then release the active drug moiety in the intracellular compartment. This leads to induction of cellular apoptosis, thus reducing systemic side effects (Wang and Low, 1998; Y. Wang et al., 2010).

The most important criteria for any drug-delivery vehicle for *in-vivo* applications are that, they must be stable to overcome the hydrodynamic fluid pressure as well as endothelial surface charges. These properties prevents undue accumulation and interaction with the physiological *milieu* which hinders the nanocargo to reach towards its destined cells. Nevertheless, these properties are important but they are not sufficient to exhibit antitumor action. The intracellular drug-delivery is possible only through various stimuli such as pH, temperature or ligand-receptor interaction (Glangchai et al., 2008; Rejinold et al., 2011; Tang and Pan, 2008). For example, certain cancer cells overexpress folate receptors on their surface, hence using folic acid (**Fa**) moieties on the surface of the vehicle can help in synaphic delivery (Guo et al., 2011; Low and Antony, 2004; Sonvico et al., 2005). Moreover, **Fa** is non-toxic, non-immunogenic in nature and stable and finally imparts negative charge on the surface, thus leading to reduced agglomeration with endothelial cells which are also

negatively charged (Sun et al., 2006; Ying Wang et al., 2010). Apart from **Fa**, large number of ligands can be exploited such as antibodies, peptides and aptamers (Cirstoiu-Hapca et al., 2007; Leuschner et al., 2006; Veisoh et al., 2009; Yigit et al., 2008).

There are many applications of the **Fe@A** complex, such as drug-delivery, MRI and hyperthermia. Even though, **MNPs** is present in the core of the NPs complex it can exhibit T<sub>2</sub> contrast MR imaging. They are emerging as a nanoplatform for multimodal imaging. Such particles have finally led to diagnostic as well as therapeutics. Moreover, such **MNPs** also possess hyperthermal property. This has led to combination therapy, where the cytotoxicity of cells are due to both drug as well as heat generated by hyperthermia. This heat also enhances the drug release and furthermore causes enhanced killing. In this research, we have reported a synthesis of gold coated magnetic (**Fe@A**) core-shell NPs for their applications in drug-delivery, MRI and microwave (MW) based hyperthermia (Fig. 1). The cytotoxicity assays of such NPs were performed on both L6 and Hep2 cells. These particles were also used for the attachment of **Fa** & Doxorubicin (**Dox**) and the drug release studies were done at different pH 5.4, 6.8 and 7.4. The stability of these NPs were also studied using zeta ( $\zeta$ ) potential. MR Imaging and Hyperthermia studies of such particles were done and was analyzed in details.

## 2. Materials and methods

### 2.1. Materials

Ferric chloride hexahydrate (Fe<sup>3+</sup>), Ferrous chloride tetrahydrate (Fe<sup>2+</sup>), sodium hydroxide (NaOH), Gold (III) chloride trihydrate (Au), L-Ascorbic acid (L-Aa), Dimethyl sulfoxide (DMSO), Hexadecyltrimethylammonium bromide (CTAB), Folic acid (**Fa**), *N*-Hydroxysuccinimide (NHS), *N,N'*-Dicyclohexylcarbodiimide (DCC), Triethylamine (TEA), Doxorubicin hydrochloride (**Dox**), MTT [3-(4,5-dimethylthiazol-2-yl) 2,5-diphenyltetrazolium bromide], Hoechst stain, Phalloidin-rhodamine B isothiocyanate, hexane and ethanol were purchased from Sigma-Aldrich. Dulbecco's Modified Eagle Medium (DMEM), fetal bovine serum (FBS), and

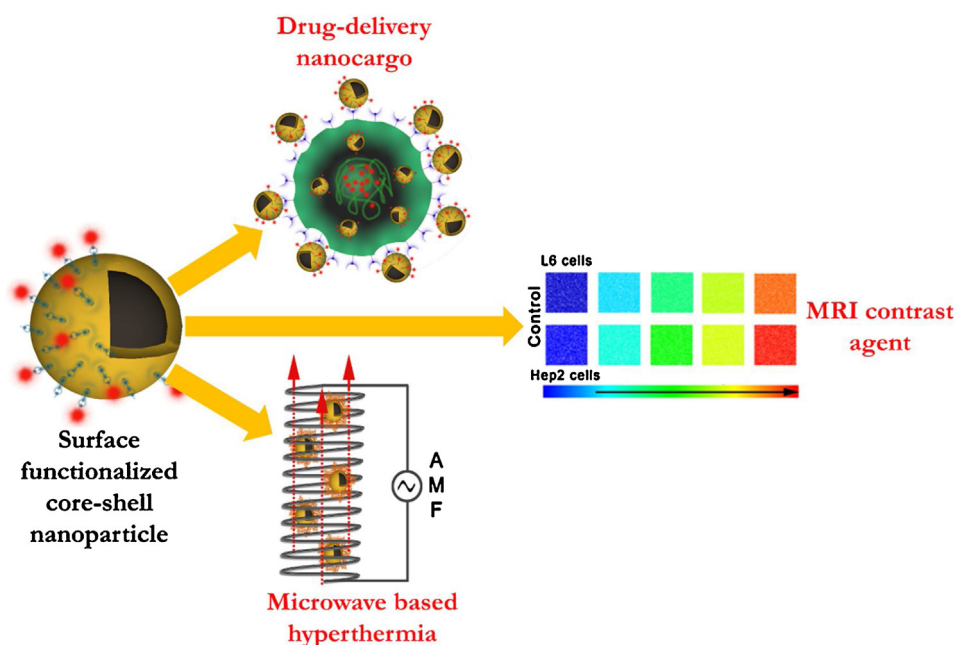


Fig. 1. Schematic representation of CSNPs tri-pronged applications.

streptomycin were obtained from Life Technologies. Agarose was purchased from Invitrogen. Deionized water (DIw) was used for all experiments and chemicals were used directly.

## 2.2. Synthesis protocols of nanoparticles (NPs) and its complexes

### 2.2.1. Magnetite (Fe) NPs

The co-precipitation method was employed to synthesize **Fe** NPs. The precursors of  $\text{Fe}^{3+}$  (0.5 M) and  $\text{Fe}^{2+}$  (0.25 M) taken in the ratio of 1:0.5 and dissolved in 50 ml of NaOH (1.5 M) in nitrogen ( $\text{N}_2$ ) degassed DIw. The reaction was carried out for 1 h at 75 °C. The resultant black NPs were separated by centrifugation and the pellet was washed 3 times with DIw. This pure **Fe** NPs were used for **CSNPs** formation.

### 2.2.2. Post-treatment of Fe NPs (solution 1)

The as-synthesized **Fe** NPs (200  $\mu\text{l}$ ) were dispersed in a mixture of 1 ml of DIw and 400  $\mu\text{l}$  of DMSO and stirred continuously in the presence of  $\text{N}_2$  atmosphere at 75 °C for 4 h in order to reduce the NPs aggregation.

### 2.2.3. Synthesis of Au seed solution (solution 2)

The freshly prepared gold seed solution was used for Au shell coating. The seed solution was prepared by using 0.5 ml (1 M, CTAB), 1 ml (50 mM, L-Aa), & 100  $\mu\text{l}$  (1 M,  $\text{HAuCl}_4$  solution). The whole complex was sonicated for 30 mins.

### 2.2.4. Synthesis of Fe@A CSNPs

**Fe@A CSNPs** were synthesized using **solution 1** and **2**. Initially, solution 2 was added dropwise to the solution 1. This mixture was stirred for 2 h until the solution colour turns purple. Then, using strong magnets the **CSNPs** were separated and washed using a mixture of hexane and ethanol to exclude excess Au NPs. The washed **CSNPs** were centrifuged to remove excess CTAB.

### 2.2.5. Activation & attachment of Fa to Fe@A CSNPs

Before attachment, the **Fa** was activated is required in order to trigger the carboxylate group by dissolving **Fa** (0.25 g) into 20 ml of DMSO under sonication to ensure complete dispersion. Later, carboxylate group present in **Fa** was activated by mixing 0.125 gm of DCC and 0.225 gm of NHS. The whole process was carried out under  $\text{N}_2$  atmosphere at 30 °C for 12 h. The resultant product was filtered using Whatman filter paper and further used. The attachment process was done by mixing 1 ml of activated **Fa** with 10 ml of **CSNPs** by stirring under  $\text{N}_2$  atmosphere for 5 h. Then, the reaction was continued for 24 h under ambient atmosphere. Finally, the dialysis process was carried out using 3000 Da dialysis membrane to eliminate excess **Fa** in PBS (pH 7.4) for 24 h. Then by centrifugation technique, the pellet was collected and again dialyzed in DI water for a period of 24 h to ensure there is no free **Fa** in the NPs system.

### 2.2.6. Loading of dox onto Fa-Fe@A CSNPs complex, drug loading efficiency and in-vitro release

To load **Dox**, 1 ml TEA, 2 ml DMSO, 5 ml **Fa-Fe@A** was mixed with 250  $\mu\text{l}$  of 5 mM **Dox** solution under  $\text{N}_2$  with continuous stirring for 5 h at 60 °C. Finally, using dialysis membrane of 3000 Da the excess **Dox** is removed in a period of 24 h. The loading efficiency of **Dox** was calculated which was found to be 94.93% before beginning the drug release studies and the calculation is shown in the ESI. *In-vitro* **Dox** release studies was carried out using dialysis membrane procedure of pH 5.3, 6.8 and 7.4 (PBS) at 37 °C under stirring. To begin this study, initially, 1 ml **Dox-Fa-Fe@A** complex is diluted with 25 ml of PBS. Then, at respective time period, 1 ml of sample was withdrawn with PBS compensation

with the same equivalent volume. The withdrawn **Dox** sample were determined at 485 nm using UV-vis spectrophotometer to evaluate the release at various time periods. The experiments were repeated three times for all the samples.

### 2.2.7. Cell culturing technique & cell viability studies

L6 – skeletal muscle cell line and Hep2 – laryngeal carcinoma cell lines were cultured in DMEM medium along with FBS (10%), penicillin (100  $\text{U mL}^{-1}$ ), and streptomycin (100  $\mu\text{g mL}^{-1}$ ) at 37 °C with a 5%  $\text{CO}_2$  atmosphere.

To evaluate cell viability, both L6 and Hep2 cells were cultured into a 24-well plate with  $1 \times 10^5$  cells/plate and incubated for 24 h. Later, the DMEM was substituted with various concentrations of respective NPs and its complexes in the range of 50–250  $\mu\text{g/mL}$ . Then the plates were incubated for 24 h and MTT-assay was executed by adding 10  $\mu\text{l}$  of MTT (5 mg/ml) in DMEM and incubated for 3 h. Then the absorbance was recorded at 490 nm using an iMark microplate reader in triplicates and the average values were considered.

### 2.2.8. Confocal microscopy studies

The cellular and nuclear morphology of both L6 and Hep2 were visualized by confocal microscopy to evaluate the impact caused by NPs and its complexes. Cells were seeded on 13 mm glass coverslips in 12-well plate with a density of  $1 \times 10^3$  cells. After incubating for 24 h, the cells were given PBS wash to remove excess or unbound NPs with media replacement. The cells were fixed using 2% paraformaldehyde. After washing with PBS, the cells are permeabilized with PBS-triton (500  $\mu\text{l}$ , 0.1%). Finally, the staining was carried with 300  $\mu\text{l}$  of Hoechst (1:4000 dilution in  $1 \times$  PBS) and Phalloidin/Rhodamine dye. To observe under confocal microscopy the vectashield was employed to fix the coverslips on the sterile glass slides.

### 2.2.9. Characterization

The UV absorption spectra of samples were measured using UV-vis spectrometer (UV-2401PC Shimadzu). X-ray diffraction (XRD) pattern using **Fe@A CSNPs** thin film were obtained on an XRD measurement (X'Pert PRO spectrometer – PANalytical) using  $\text{Cu K}\alpha$  radiation ( $k\alpha = 0.154 \text{ nm}$ ). The morphology and confirmation of **CSNPs** formation were characterized using a transmission electron microscope (TEM JEM-ARM200F, Jeol) with their related techniques such as HRTEM (High Resolution Transmission Electron Microscope), HAADF-STEM (high-angle annular dark-field scanning transmission electron microscopy) detector and EDS (Energy Dispersive X-Ray Spectrometer) (Oxford XMax 80). The NPs in cell internalization was analyzed using CryoEM (Tecnai F20, FEI). The surface composition studies were carried out using XPS (X ray Photoelectron Spectrometer) (K-Alpha Surface Analysis, Thermo Scientific). The surface charge of NPs were studied in a Zetasizer Nano ZS90 (Malvern Instruments). The loading of **Fa** and **Dox** were evaluated using Fourier-transform infrared (FTIR) spectra were made on a Nicolet iS50 spectrometer (Thermo Scientific). The stability of NPs and its complexes at higher temperature were done using TGA (Thermogravimetric Analysis) (Q50 TA Instruments) from 30 to 900 °C. Magnetic measurements were achieved on a superconducting quantum interference device (SQUID), (Quantum Design, MPMS3). The cellular morphology was visualized using confocal microscopy (Zeiss LSM 700).

2.2.9.1. *Magnetic resonance imaging (MRI) phantom preparation.* L6 and Hep2 cells were labelled with **Fe@A CSNPs** and dispersed with pre-heated 0.5% agarose gel of 1.5 ml at 40 °C and slowly allowed to cool down to solidify which is stored at 4 °C until the MR imaging studies. For control, the agar gel with the cells are considered.

2.2.9.2. *MRI experiments.* Both  $T_1$  &  $T_2$  contrast studies were obtained using 7 T scanner (Signa HDxt, Varian). The following parameters were employed,

- $T_1$  measurements: Coronal spin-echo sequences with TE = 25 ms and repetition time from 25 ms to 6 s were used.
- $T_2$  measurements: Fast spin echo sequence with TR = 2000 ms, FOV = 3\*3 cm, TE = 15–250 ms, slice thickness of 4 mm and resolution of 256 × 256.

### 2.2.9.3 MW based Hyperthermia experimental setup:

The pre-assembled home-made setup was used to study the MW based hyperthermia studies at 2.45 GHz. The home-made MW experiment setup consists of following components:

- Frequency generator (2.45 GHz) – SML 03, Rhode & Schwarz,
- MW signal amplifier – 1164-BBM3Q6AHM, Empower,
- Monitoring output power – DC7154 M, Amplifier Research,
- Monitoring 6W output power and reflected power – PM2002, Amplifier Research,
- Adjusting the standing wave ratio (SWR) – coaxial stub tuner 1878C, Maury Microwave Corp and network analyzer – E5071B, Agilent Technologies.

The temperature change in the sample was measured using optical fiber sensors (M3300, Luxtron).

## 3. Results and discussions

### 3.1. Mechanism involved in the synthesis of core/shell nanoparticles (CSNPs)

**MNPs** synthesis (core) occurs when  $Fe^{3+}$  and  $Fe^{2+}$  reaches its critical supersaturation value causing short burst of nucleation. The reaction kinetics of such nuclei formation at 80 °C is purely a temperature-dependent mechanism, in which the diffusion of ions takes place from the bulk phase to the surface of nuclei (Peterson et al., 2002). This growth step is followed by agglomeration due to Ostwald ripening which finally leads to reduction of overall energy of the system. Dimethyl sulfoxide (DMSO) stabilizes **MNPs** due to surface negative charge on them causing repulsion, thus preventing agglomeration of the particles (Vijayendran and Leckband, 2001). To circumvent the problem of oxidation in air, an inert layer of Au nanoshell is encapsulated on the surface of **MNPs**. **MNPs** exhibit misalignment of spins on the surface. When gold interfacial layer is overlaid on such a disordered surface, there is further increment in the spin disorderness thus influencing the magnetic properties of **MNPs** (Dijk et al., 2006).

The **CSNPs** synthesis involves a seed mediated approach constituting CTAB, Au ions and a mild reducing agent, AA. The reaction sequence involves metallomicelle formation by  $AuCl_4^-$  with CTAB to form  $CTA^+AuBr_4^-$ , which is orange coloured solution. As  $AuBr_4^-$  has lower potential as compared to  $AuCl_4^-$  it is difficult for weak reducing agent such as AA to reduce  $AuBr_4^-$  to form Au atoms. AA can only reduce  $AuBr_4^-$  in the metallomicelle to form  $AuBr_2^-$ , which is light violet coloured solution. The first reduction reaction occurs in the metallomicelles within the Au seed solution, while the second reduction reaction occurs on the surface of **MNPs**. At room temperature, the second reduction reaction cannot form a uniform shell on the surface of **MNPs** core hence a mild temperature of 80 °C is required to form a uniform outer layer. Brown coloured magnetic particles became dark purplish when light violet coloured Au seed solution was mixed with it. The Au seeds supply large number of small randomly oriented crystalline domains along with particle mediated electron transfer, thus

facilitating the Au shell on the surface of **MNPs** (Robinson et al., 2010).

### First Reduction : $Au^{3+} \rightarrow Au^{1+}$



### Second Reduction : $Au^{1+} \rightarrow Au^0$



### 3.2. Structural characterizations of CSNPs

XRD patterns of **CSNPs** is displayed in Fig. 2. The characteristic peaks of pure **GNPs** (JCPDS file numbers: 004-0784) were compared with the **CSNPs** (Karaagac et al., 2010). The XRD pattern demonstrated a strong peak at  $2\theta = 38^\circ$ , which is a signature marker for Au, which correspond to Miller Index (111) respectively. The Au peaks were dominant in XRD due to the heavy atom effect. Since Au is heavier than iron, all the other peaks of **MNPs** were suppressed (Fan et al., 2005; Okahata et al., 1998; Yu et al., 2004). From the XRD data, we also calculated the size of the NPs using the Scherrer formula (Schroder et al., 2006):

$$D_p = \frac{0.94\lambda}{\beta_{1/2} \cos\theta} \quad (3)$$

The average diameter of the NPs calculated using the above formula was estimated to be 14 nm, which was corroborated by TEM. In order to confirm the gold shell formation, the absorption spectra of SPR peak was monitored using UV–vis spectroscopy. The deposition of Au seeds onto the metallic Fe core leads to a red-shift of the SPR peak to 581.5 nm (Fig. 2 inset) which proves the **CSNPs** (Xu et al., 2007).

Transmission electron microscopy (TEM) of **Fe@A** demonstrated an average size of the particles in the range of 11 nm (Fig. 3a, Histogram subset). The particles were nearly monodisperse and spherical. **CSNPs** typically exhibit no agglomerations due to very

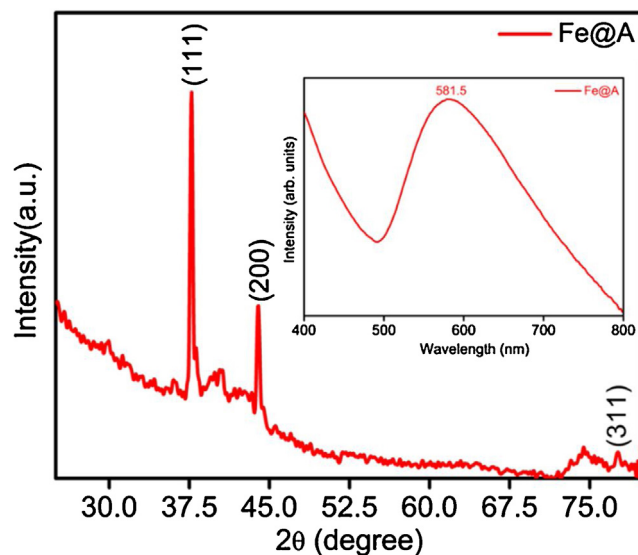
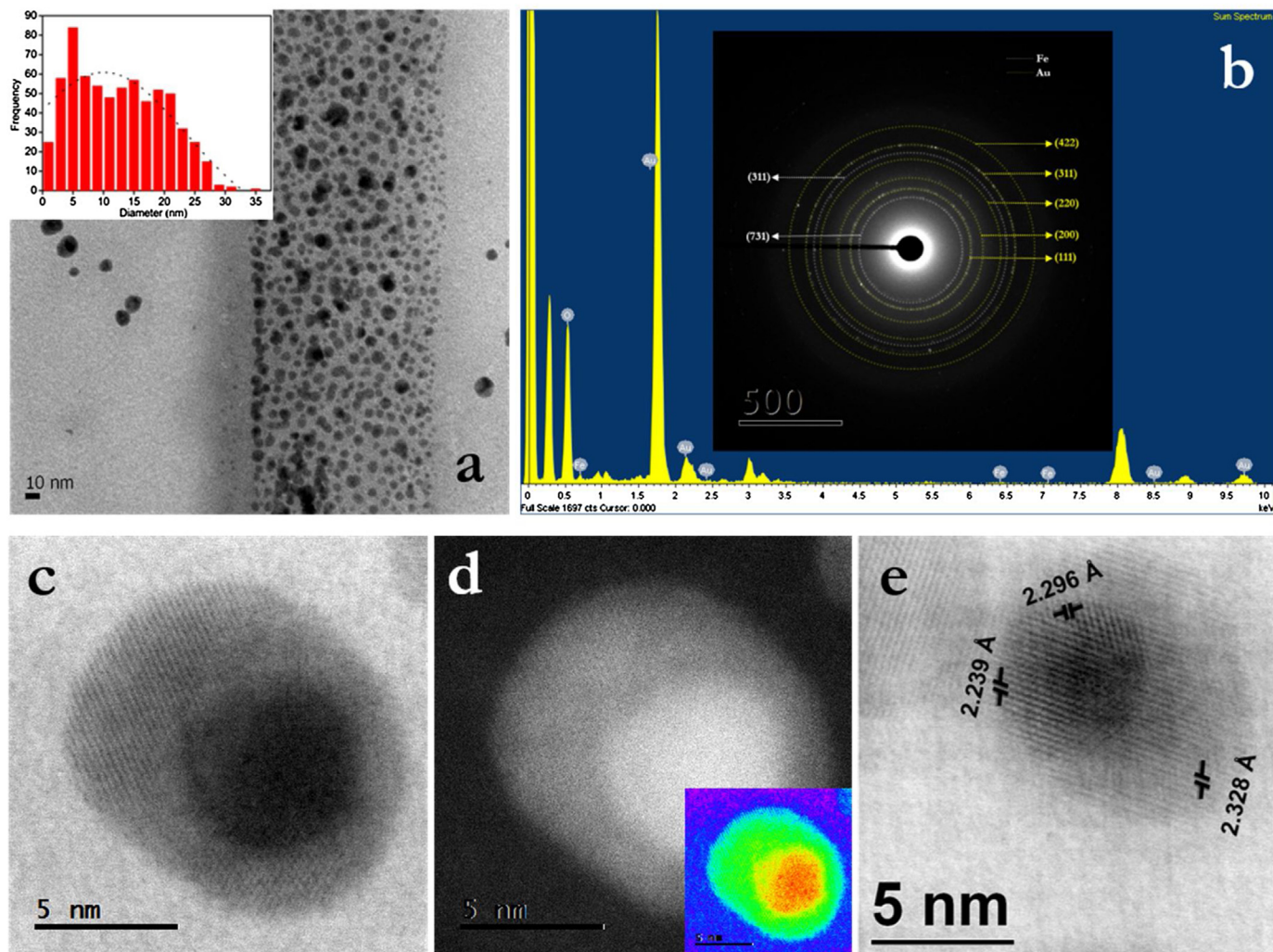
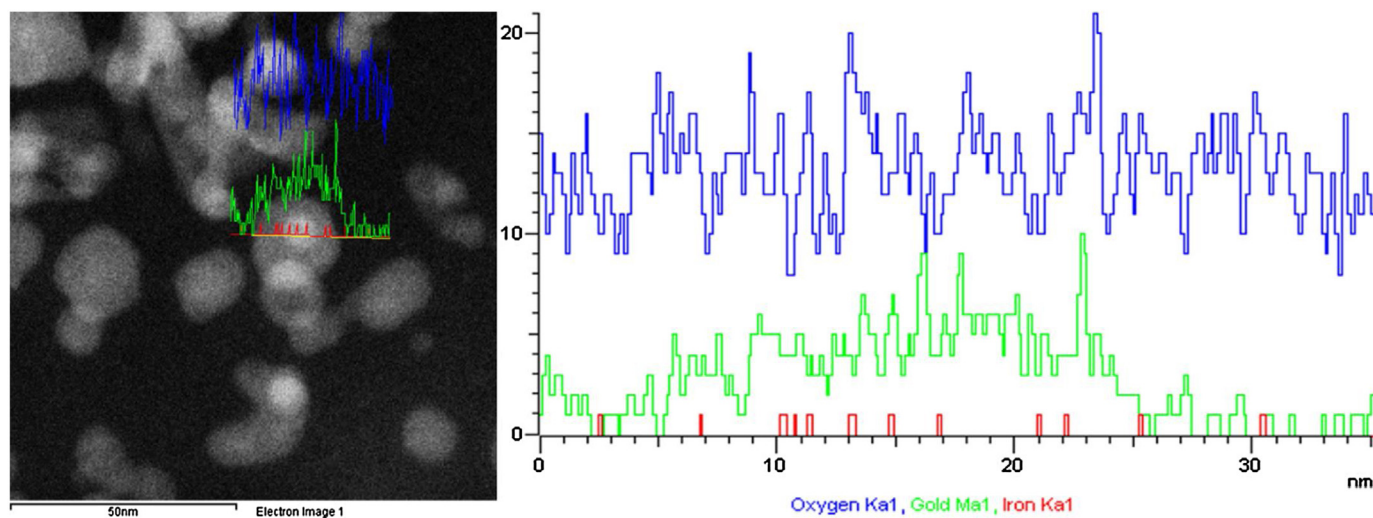


Fig. 2. XRD pattern for the **CSNPs** showing characteristic peaks at (111), (200) and (311) for Au, inset represents the SPR peak of **CSNPs**.



**Fig. 3.** (a) TEM micrograph of CSNPs exhibiting monodisperse NPs of size 5–20 nm (Histogram in subset), (b) EDAX showing the presence of Au, Fe and O (Inset: SAED pattern from CSNPs, showing a superposition of Au and Fe lattices), (c), (d) HAADF imaging, maps the CSNPs Gold/Iron oxide NPs (Inset: RGB colour display clearly indicates the formation of CSNPs based on the difference in the colour contrast), (e) measurement of the lattice distances.



**Fig. 4.** Line mapping of CSNPs indicating the core of iron and shell of gold.

low free surface energy (Thaxton et al., 2003). HRTEM of the **Fe@A CSNPs** revealed discrete separation between the Fe and Au phases, which is a clear indication of unique incorporation of Au shells on the surface of **MNPs**, as reported previously (Aslan et al., 2005). The diffusion of Au into Fe leads to the formation of metastable Au-Fe phase (Thanh and Green, 2010). Due to the curvature effect, there is distortion in the crystal lattice on the surface of the NPs. The average diameter of **CSNPs** was increased to 11 nm from 6 nm of iron oxide seeds when gold chloride was reduced on its surface. Hence, the average thickness of the gold nano-shell was 5 nm, suggesting that the addition of Au on the surface of the NPs consequently increased the diameter of the NPs.

The number of shells of gold formed on iron oxide was calculated using the following formula:

$$\begin{aligned} \text{No. of shells formed} &= \frac{\text{Thickness of Aushell}}{\text{Atomic diameter of gold}} \\ &= 5/0.2 = 25 \text{ shells} \end{aligned}$$

Thus, around 25 shells of Au on average encapsulate each **MNPs**. These shells stabilized by CTAB confer a positive charge on the particles depicted from the Zeta potential values in Table S1 (in the ESI).

This leads to further enhancement of the stability of NPs due to the electrostatic force of repulsion existing between the particles. EDAX results shown in Fig. 3b indicated particles comprised mainly three atoms: Fe (39.63%), Au (37.57%) and O (22.8%). Fig. 3b inset represents the SAED pattern of **Fe@A** which is an overlapping of both Au and Fe lattices with distinguishable planes of majorly Au (Huang et al., 2011). The HAADF imaging of **CSNPs** using STEM mode in Fig. 3c and d demonstrated the intertwined MNPs, which were overlaid by Au nanoshells. The HAADF image was highly sensitive to the changes in the atomic number of atoms in the sample (Z-contrast images) due to very high angle, incoherently scattered electrons. The dark inner core as compared to lighter outer shell (Fig. 3c) was due to the dominating mass contrast over diffraction contrast, thus making the shell lighter even if Au had a higher electron density than Fe. The red-green-blue (RGB) colour display shown in Fig. 3d inset clearly indicated the formation of **CSNPs** based on the difference in the colour contrast. The measurement of the lattice distances in Fig. 3e revealed the evidence of the crystal plane (311) inside the core, thus indicating the presence of magnetite as well as planes (316) and (209), thus indicating the presence of maghemite. The presence of maghemite indicates that there is partial transformation of magnetite, resulting in the change in oxidation states of Fe. Furthermore, the shell constituted of (111) crystal plane which is a signature

marker of Au. Fig. 4. also shows line mapping of **CSNPs**, which confirmed the core of iron and shell of Au.

### 3.3. Magnetic characterizations

Fig. 5. displays the plots of magnetization versus magnetic field at 5, 300 and 312 K for the **Fe@A CSNPs**. Saturation magnetization of **CSNPs** was 80.9 emu/g at 5 K and 53.2 emu/g at 312 K. These values were markedly lower than the saturation magnetization of bulk Fe NPs (92 emu/gm) (Rao et al., 2007; Tiller, 1991). The reduction in the saturation magnetization may be due to the decreased particle size (Luzar and Chandler, 1993). The overall magnetism of the **CSNPs** displayed decreased saturation magnetization due to the incorporation of non-magnetic Au shell to the inner core. Furthermore, decrement in coercivity ( $H_c$ ) also resulted due to the decrease in magnetic surface anisotropy as a consequence of Au shell formation (Murphy et al., 2010).

### 3.4. Surface composition of Fe@A

The important criteria for the synthesis of **CSNPs** is usually the completeness of shell onto the surface of core NPs (Goon et al., 2009). Therefore, to confirm this criteria XPS was employed for evaluating the surface composition of **Fe@A** as shown in Fig. S1 (in the ESI). Analysis of the individual elemental XPS spectrum confirmed the oxidation states of each elements in the solution. Fig. 6a shows two dominant peaks at 710.8 and 724.5 eV which is a signature marker of Fe (2p<sub>3/2</sub>) and Fe (2p<sub>1/2</sub>), respectively. These two peaks consist of Fe<sup>2+</sup> and Fe<sup>3+</sup> of FeO and Fe<sub>2</sub>O<sub>3</sub> peaks respectively of Fe<sub>3</sub>O<sub>4</sub> NPs (Barr, 1978). And the satellite peak at 718.9 eV was ascribed to Fe<sup>3+</sup> ions. There is a minor blue-shift of Fe (2p<sub>3/2</sub>) peak from 711.2 to 710.8 eV which confirms a very strong electronic interface between Fe core and Au shell (Tu, 2008). Fig. 6b represents the XPS of Au spectra of the **CSNPs**. The two peaks at 83.99 and 87.65 eV relates to Au (4f<sub>7/2</sub>) and Au (4f<sub>5/2</sub>), respectively. These results confirms that the emission of 4f photoelectrons from Au<sup>0</sup> (Jaramillo et al., 2003), which suggest the presence of Au<sup>0</sup> atoms on the Fe core NPs (Lo et al., 2007) also with the absence of Cl (2p) ions (Fig. 6c) confirming the deposition of Au onto the Fe NPs. Even after the coating of Au onto the Fe, detection of Fe atoms is possible it may be due to thin Au coating of 5–10 nm (Ratner and Castner, 2009), or Fe atomic surface were exposed during the analysis (Goon et al., 2009). The C (1s) binding energy was used as an internal reference for the analysis (Fig. 6d). The O (1s) peaks is can be deconvoluted into two peaks at 530.1 and 532.7 eV which corresponds to O–Fe of Fe (Hui et al., 2004), and O–C of carboxyl group (Mohapatra and Pramanik, 2009; Vogelson et al., 2003) (Fig. 6e).

### 3.5. Surface modification using Fa and dox onto the Fe@A surface

The efficiency of NPs based targeting or therapy depends on the efficacy of drug released in the specific target tissue which is purely based on the surface functionalization of NPs. These modifications aids in receptor mediated targeting which is a common strategy to increase the efficacy of drug (Řihová, 1998; Swaan, 1998). The receptor mediated is majorly contributed by folic acid (**Fa**) to target cancer cells/tissue for specific delivery. **Fa** is a vitamin (Cezar et al., 2007) which is very essential for the nucleoside synthesis (Ross et al., 1994; Weitman et al., 1992). So cancer cells overexpress the folate receptors (Gabizon et al., 1999), which has high affinity towards **Fa** on the cell surface (Lu and Low, 2012). Additionally, these **Fa** is non-immunogenic, stable, and has small molecular size which can easily internalize the NPs through cellular membrane (El-Hammadi et al., 2017; Hijaz et al., 2016; Rana et al., 2016; Sadhasivam et al., 2015; Stella et al., 2000; Su et al., 2014; Zarrin

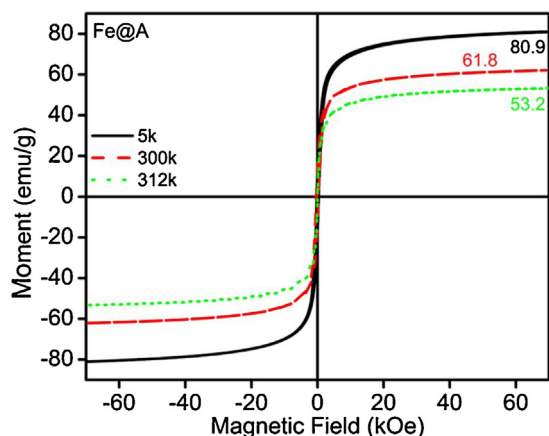


Fig. 5. Magnetization of the **Fe@A** using SQUID at 5, 300 & 312 K.

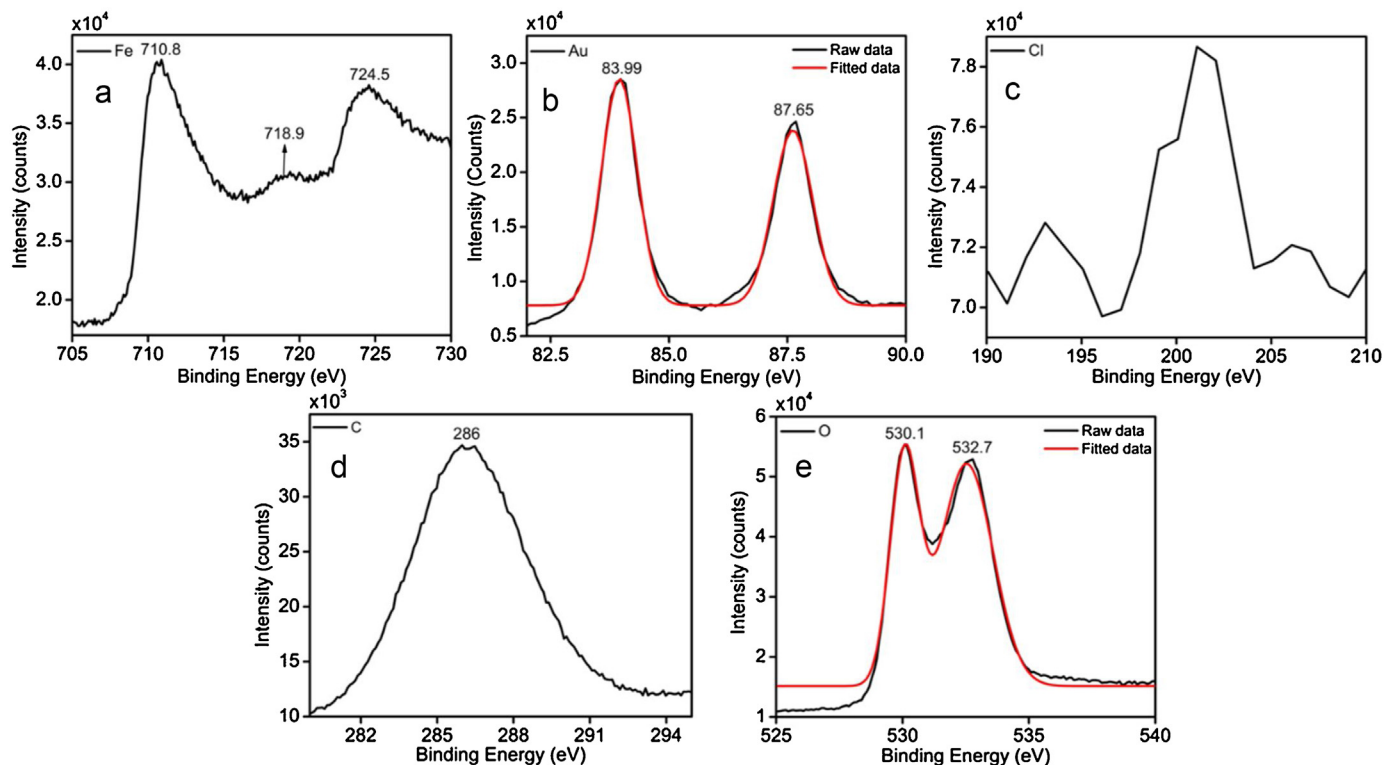


Fig. 6. Elemental analysis of Fe@A by XPS which clearly shows the presence of elements such as (a) Fe, (b) Au, (c) absence of Cl, (d) C, and (e) O.

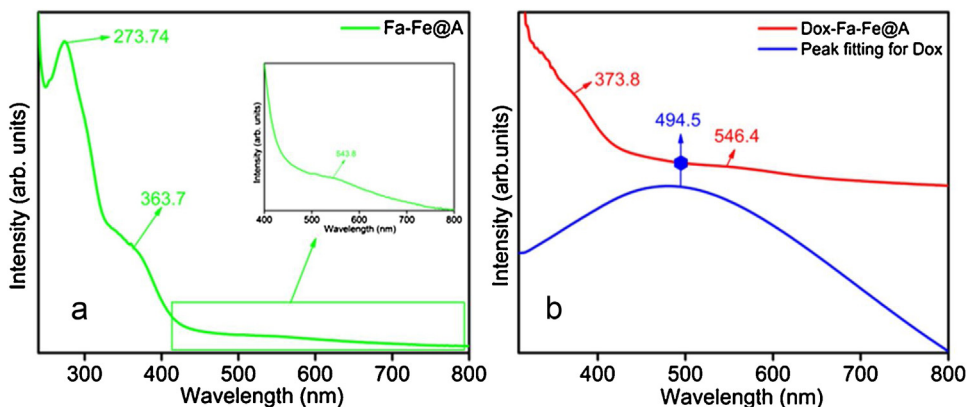


Fig. 7. (a) UV-vis spectra of Fa functionalization and (b) loading of Dox onto Fa-Fe@A.

et al., 2016; Zhang et al., 2015). Thus we developed an efficient NPs-Fa conjugate complex for the following applications.

The UV-vis absorption spectra of the Fa-Fe@A in aqueous solution is shown in Fig. 7a. The SPR peak of the Fe@A and peak of Fa are observed. The absorption spectrum of Fa-Fe@A displayed the characteristic absorption peaks of the Fa (273.74 and 373.8 nm) (Dántola et al., 2010), indicating the conjugation of Fa onto the surface of the Au shell. And due to SPR property the Au expresses the peak at 543.8 nm. This confirms the formation of Fa complex.

The grafting of Dox onto Fa-Fe@A was confirmed by UV-vis spectra which is represented in Fig. 7b. In this spectrum, the three major peaks are observed. In case of Fa, the weak hump is seen at 373.8 nm and the signature marker at 273.74 nm disappears because of the loading of Dox. For, Fe@A the absorption is seen at 546.4 nm showing minor red-shift from the previous spectrum and finally we have employed origin software to carry out the peak fitting (blue hexagon) for Dox which is observed at 494.5 nm with

slight red-shift from 485 nm (X. Chen et al., 2014) due to the conjugation with Fa by amide bond (Ravichandran et al., 2016) which is confirmed by FTIR. Therefore, this spectrum confirms the complex formation is successful which can be employed for further applications.

Chemical structures of Fa and Dox attachment onto Fe@A CSNPs were investigated by FTIR spectroscopy. Fig. 8a represents the FTIR bands of CTAB and Fa loading on the surface of Fe@A. The intensity of CTAB peaks are clearly shown because in most of the cases the peak intensities are purely depend on the metal NPs shape and size (Honary et al., 2013). The peaks are shifted from the standard FTIR peaks of CTAB (Ede et al., 2014) which is compared in Table 1. This confirms that the CTAB aids in capping of Au NPs.

The Fa attachment was confirmed by comparing with the characteristic peaks of pure Fa (Zhang et al., 2008). From the spectra, 5 major bands are obtained which is slightly shifted from the standard Fa. These proves that Fa has been successfully

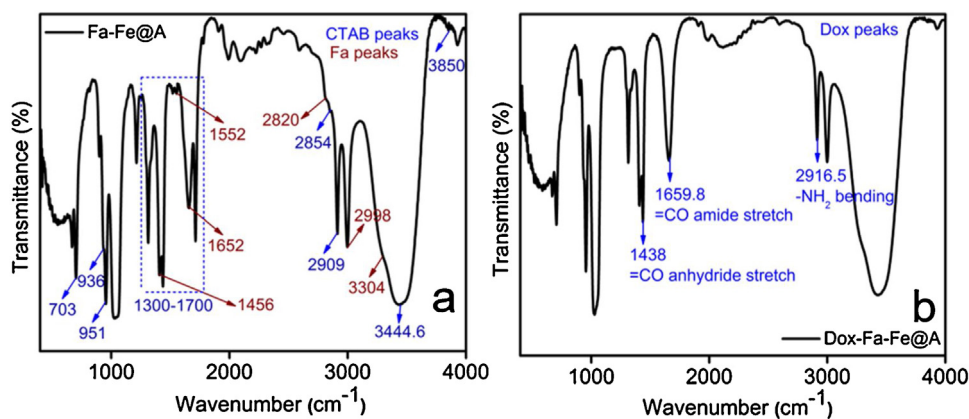


Fig. 8. FTIR spectra showing the attachment of (a) **Fa** and (b) **Dox** onto **Fe@A**.

Table 1

FTIR peaks for CTAB (standard and observed) and its assignment.

Assignment	CTAB peaks Standard (cm <sup>-1</sup> )	Observed (cm <sup>-1</sup> )
CH <sub>2</sub> scissoring & O–H bending	1300–1680	1300–1700
C–H stretching	2846	2854
C–H anti-stretching	2932	2909
N–H stretching	3330–3460	3444.6
O–H stretching	3750	3850

attached onto the surface of NPs forming a complex of **Fa-Fe@A**. In particular, the 3 significant peaks of **Fa** at 1456 (–NH<sub>2</sub>), 1560 (–NH), and 1652 cm<sup>-1</sup> (–CONH) were seen (Yuan et al., 2010).

Fig. 8b shows the FTIR spectra of **Dox** immobilization onto **Fa-Fe@A**. The spectra is plotted separately to avoid the overlapping of **Dox** peaks [1438 cm<sup>-1</sup> (=CO anhydride stretch), 1659.8 cm<sup>-1</sup> (=CO of amide stretching), 2916.5 cm<sup>-1</sup> (–NH<sub>2</sub> bending)] with the peaks of CTAB and **Fa**. It is inferred that the intensity of CTAB peaks has been reduced majorly proving that the exposure is less due to immobilization of more **Dox**. The **Dox** loads with **Fa** by means of –CONH bond by the conjugation between –NH<sub>2</sub> of **Fa** attached **Fe@A** and –COOH of **Dox** (Pandey et al., 2013a).

### 3.6. Stability and zeta potential studies of NPs

TGA was performed to confirm the thermal stability and step by step surface modification of the NPs under N<sub>2</sub> atmosphere is shown in Fig. 9a. The NPs samples were heated upto 900 °C, and the % weight loss of **Fe**, **Fe@A**, **Fa-Fe@A**, and **Dox-Fa-Fe@A** were 56%, 11.06%, 9.7%, and 0.9%, respectively. In TGA analysis, the curves are majorly divided into two segments: initial weight loss is due to

dehydration, and later is produced by decomposition of organic/metal complexes (Huang et al., 2015). From the thermograms figure, the initial weight loss for all samples of less than 200 °C is ascribed to water, precursors and solvent residues (J. Chen et al., 2014) from the particle synthesis are removed.

In case of **Fe**, a thermo-magnetometric study shows that at 270 °C maghemite is formed, and above 320 °C hematite is formed due to high temperature (Sanders and Gallagher, 2003). But the oxidation of **Fe** at higher temperature is prevented by coating with Au shell forming **Fe@A**. So eventually for **Fe@A**, initially all the water and unreacted precursors are degraded (Rai et al., 2010) and maintains a plateau until 760 °C and after that the surfactant (CTAB) and ascorbic acid (AA) are decomposed completely (Basavegowda et al., 2014). This proves that a large amount of CTAB and AA were employed in the reduction and protection of Au ions.

After the attachment of **Fa**, there is a drastic drop in the curve due to the loss of surface moisture and followed by a continuous decrement with a weight loss which could be assigned to **Fa** molecule loss on the surface (Sahoo et al., 2013). Finally, the TGA curve of **Dox-Fa-Fe@A** shows a sudden drop from 50 to 106 °C which retains the same upto 785 °C and finally degraded completely. It is due to the complete organic nature of the NPs complex which is majorly exposed to **Fa** and **Dox** at high temperatures.

The zeta potential of the NPs were examined as because the stability and biocompatibility is purely depend on the NPs surface charges (Jin et al., 2016). Fig. 9b and Table S1 (in the ESI) shows zeta potential measurements as a function of pH (5.4, 6.8 & 7.4) for the **Fe**, **Fe@A**, **Fa-Fe@A**, and **Dox-Fa-Fe@A**. The core **Fe** NPs synthesized by co-precipitation showed a ζ potential of +8.8 to +14.5 mV through DMSO modification; the S=O bond in DMSO forms a

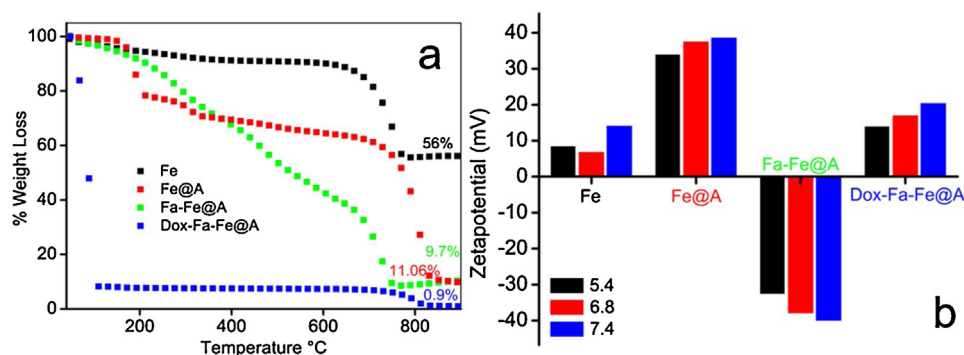


Fig. 9. (a) TGA analysis of all complexes to study the stability at higher temperatures, (b) Zeta potential of **Fe**, **Fe@A**, **Fa** functionalized **Fe@A** and **Dox** encapsulated **Fa-Fe@A**.

strong H bonds with H atoms of the NaOH (OH groups) (Shenderova et al., 2010; Zhang et al., 2014). In case of the Au coated Fe NPs, showed  $\zeta$  potential value of +34.3 to +39 mV as the consequence of positive charge imposed by CTAB capping on AuNPs (Ricles et al., 2014; Wang et al., 2013). The **Fa-Fe@A** NPs expresses a negative charge (−32.9 to −40.4 mV) which is due to **Fa**—COOH groups deprotonation (Das et al., 2008) on the NPs and the  $\zeta$  potential value is more than −32.0 mV which indicates that the NPs are very stable. Finally, the  $\zeta$  potential value of the **Dox-Fa-Fe@A** was noticed to be +14.3 to +20.8 mV as pH increases which is because of the inherent positive charge of **Dox** (Pandey et al., 2013b).

### 3.7. Fa-Fe@A NPs internalization in cells

The **Fa** attached NPs has high affinity towards overexpressed folate receptors (FR) on the cancer cells (El-Hammadi et al., 2017; Sadhasivam et al., 2015; Wang and Low, 1998; Zarrin et al., 2016). Therefore, the trafficking of the **Fa-Fe@A** NPs inside the Hep2 cell lines was examined by cryoEM analysis by incubating NPs with the media (Figure S2a in the ESI). The **Fa-Fe@A** complex entered the cells by receptor-mediated endocytosis pathway (Kamen and Capdevila, 1986; Leamon and Low, 1991). NPs cluster shown in Figure S2b in the ESI which is high magnification cryoEM represents the internalization within the cell by vesicles formation in the cytoplasm. And also observed that there is no entry of NPs in the nuclei and cytoplasmic organelles was unaffected. This confirms that the **Fa** functionalized NPs are acting as an efficient nanocargo to deliver the drugs inside the cells.

### 3.8. Evaluating cytocompatibility in L6 & Hep2 cells

The free drug – **Dox**, synthesized and functionalized NPs like **Fe**, **Fe@A**, **Fa-Fe@A**, and **Dox-Fa-Fe@A** were tested in a various range of concentrations (50–250  $\mu\text{g/ml}$ ) to evaluate their cytotoxic effects on the cell lines which is shown in Fig. 10a & b. In this study, we have employed a non-cancer (L6) and cancer (Hep2) cell lines to prove that our NPs system specifically target cancerous cells and induce the process of apoptosis by means of **Fa** attachment and **Dox** loading, which avoids the non-cancer healthy cells from drug side-effects which is usually seen in the practice of current chemotherapy treatments (Moses et al., 2003). Therefore, the cells were incubated with drug and NPs for a period of 24 h and then MTT assay was carried out to evaluate the cell viability. Both L6 and Hep2 exhibited more than 70% viability when exposed to **Fe**, **Fe@A**, **Fa-Fe@A** NPs showing minor toxicity even after exposure to

high concentrations of NPs. This indicates that these NPs does not affect both the cell lines.

In case of free **Dox**, when exposed to L6 cells, shows minor killing but the same concentration of **Dox** with Hep2 cells showed 40% cell viability. And finally, the designed nanocargo **Dox-Fa-Fe@A** with L6 cells showing 25% of cell death and with Hep2 it carried out its function by delivering the **Dox** effectively and killing the cancer cells upto 91% within 24 h. This proves that the nanocargo acts as an efficient system as an anti-cancer agent.

After MTT testing, the morphological observation of both L6 and Hep2 cells were demonstrated. Fig. 11A & B shows the confocal laser scanning microscopy (CLSM) of the cells incubated with **Fe**, **Fe@A**, **Fa-Fe@A**, and **Dox-Fa-Fe@A** for 24 h. The cellular uptake and cytotoxic effects of the NPs on the cells were studied.

#### 3.8.1. L6 cells

In case of L6 cells, the NPs complex does not shows any cytotoxic effect which can be seen by retaining the normal cytoplasmic and nuclear morphology (Fig. 11A–a–c). While, the **Dox-Fa-Fe@A** treated cells show a minor nuclear disruption due to side-effects of drug **Dox** (Fig. 11A–d). These results confirm that the NPs shows high permeability and biocompatibility so they are suitable as a nanocargos for cancer cell drug delivery.

#### 3.8.2. Hep2 cells

Meanwhile, with Hep2 cells there was major difference in the viability incubated with hybrid NPs confirmed by CLSM experiments. Similar results like L6 cells are seen that the **Fe**, **Fe@A**, and **Fa-Fe@A** (Fig. 11B–a–c) does not affect the cells. But, the huge variation is seen with **Dox-Fa-Fe@A**, (Fig. 11B–d) the Hep2 cells undergoes for apoptosis with the clear disruption of cellular and nuclear contents. This proves that the **Dox** is delivered in the nucleus and the drug does its function of initiating apoptosis and leading to cell death. Thus, the results obviously proves that the cargo can be a potential candidate for the drug delivery.

### 3.9. Applications of Fe@A

The various applications of biofunctionalized **Fe@A** CSNPs are as follows:

#### 3.9.1. Drug release and kinetics studies at different pH

Tumor microenvironment possess lower pH as compared to the normal tissue milieu (Estrella et al., 2013). The normal physiological pH is 7.4, but due to anoxic microenvironment in tumor region, there is enhanced glucose uptake and its rapid breakdown into acid

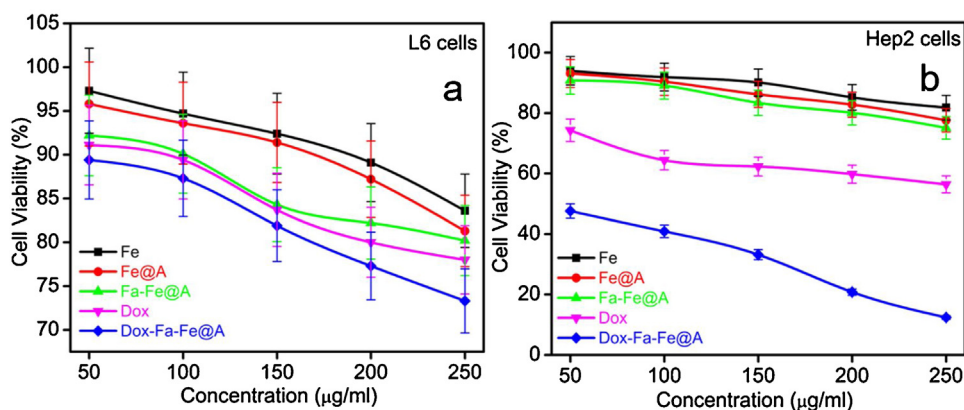
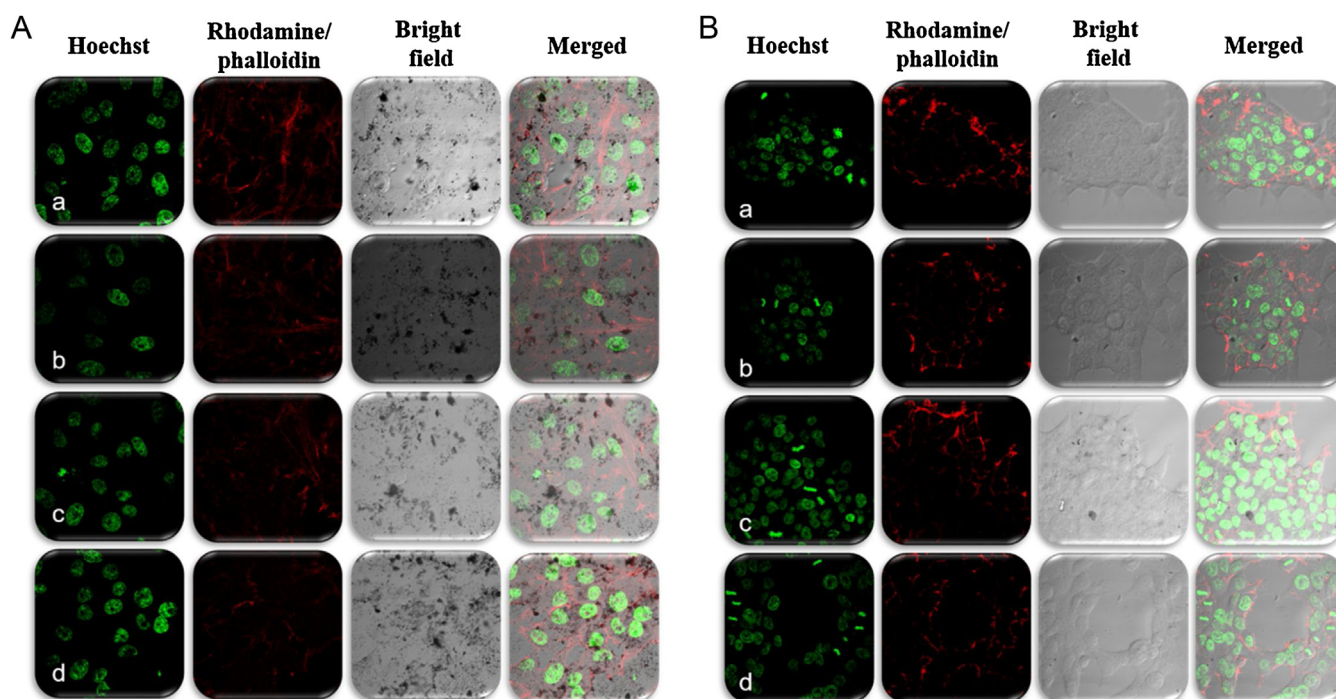
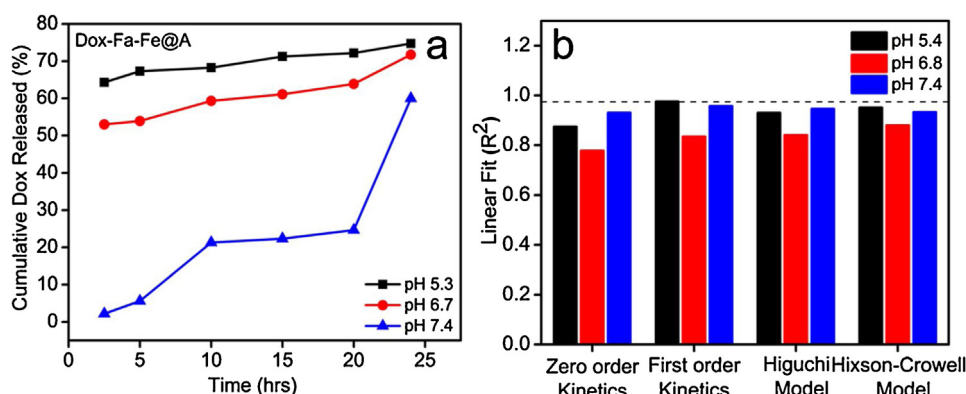


Fig. 10. MTT assay of (a) L6 cells with **Fe**, **Fe@A**, **Fa-Fe@A**, **Dox** and **Dox-Fa-Fe@A** showing no apoptosis at even at higher concentrations (b) Hep2 cells with only **Dox** and **Dox-Fa-Fe@A** showing around 91% cell death at high conc.



**Fig. 11.** (A) L6 Cell morphology analysis by confocal microscopy study treated (a) Fe, (b) Fe@A, (c) Fa-Fe@A, (d) Dox-Fa-Fe@A (Scale bar is 20  $\mu\text{m}$ ). (B) Hep2 Cell morphology analysis by confocal microscopy study treated (a) Fe, (b) Fe@A, (c) Fa-Fe@A, (d) Dox-Fa-Fe@A (Scale bar is 20  $\mu\text{m}$ ).



**Fig. 12.** (a) Cumulative release of Dox released at 3 different pH, (b) plot representing various kinetic models of drug release kinetics.

leads to the decrement of the pH of such regions to 6.8. A paradigm drug-delivery model needs to be designed in such a way that, there is maximal release at lower pH in comparison to physiological pH. Moreover, drugs like Dox becomes active in acidic environment, hence there must be maximum release in intracellular compartments, such as endosome, where pH becomes 5.4 (Rybak and Murphy, 1998). Keeping these points into consideration, the *in vitro* drug release of Dox-Fa-Fe@A was investigated by employing 3 PBS buffers at different pH (5.4, 6.8 & 7.4) at room temperature for 24 h. We determined that our NPs system is pH dependent. As the pH decreases in the cellular organelles thereby increasing the release of drugs. The Dox cumulative release at 3 different pH after 24 h was found to be 74.73% at pH 5.4, 71.74% at pH 6.8 and 59.99% at pH 7.4 (Fig. 12a). At pH 5.4 it shows the maximum amount of drug release when compared to pH 6.8 & 7.4. This difference is due to pH decrement inside the endosomes which lead to detachment of drug by breaking the bond between the molecules. The obtained

results were put into discrete drug kinetics model (Fig. 12b) and realized that they followed first order rate kinetics from the high regression coefficient value ( $R^2 = 0.9755$ ).

### 3.9.2. MR imaging using Fe@A in L6 & Hep2 cells

MR Imaging is a non-invasive method in which the active nuclei excited by radio-frequency pulse will be relaxing back to the initial ground state. This process is constituted of two components,

- longitudinal relaxation time ( $T_1$ ), and
- transverse relaxation time ( $T_2$ ),

which can be used to get an MR image (Scherzinger and Hendee, 1985). This technique helps in diagnosis of pathologies based on the positive contrast enhancement as in  $T_1$  or negative contrast enhancement as in  $T_2$ . MNPs become highly magnetized under magnetic field and possess induced magnetic fields that can lead to

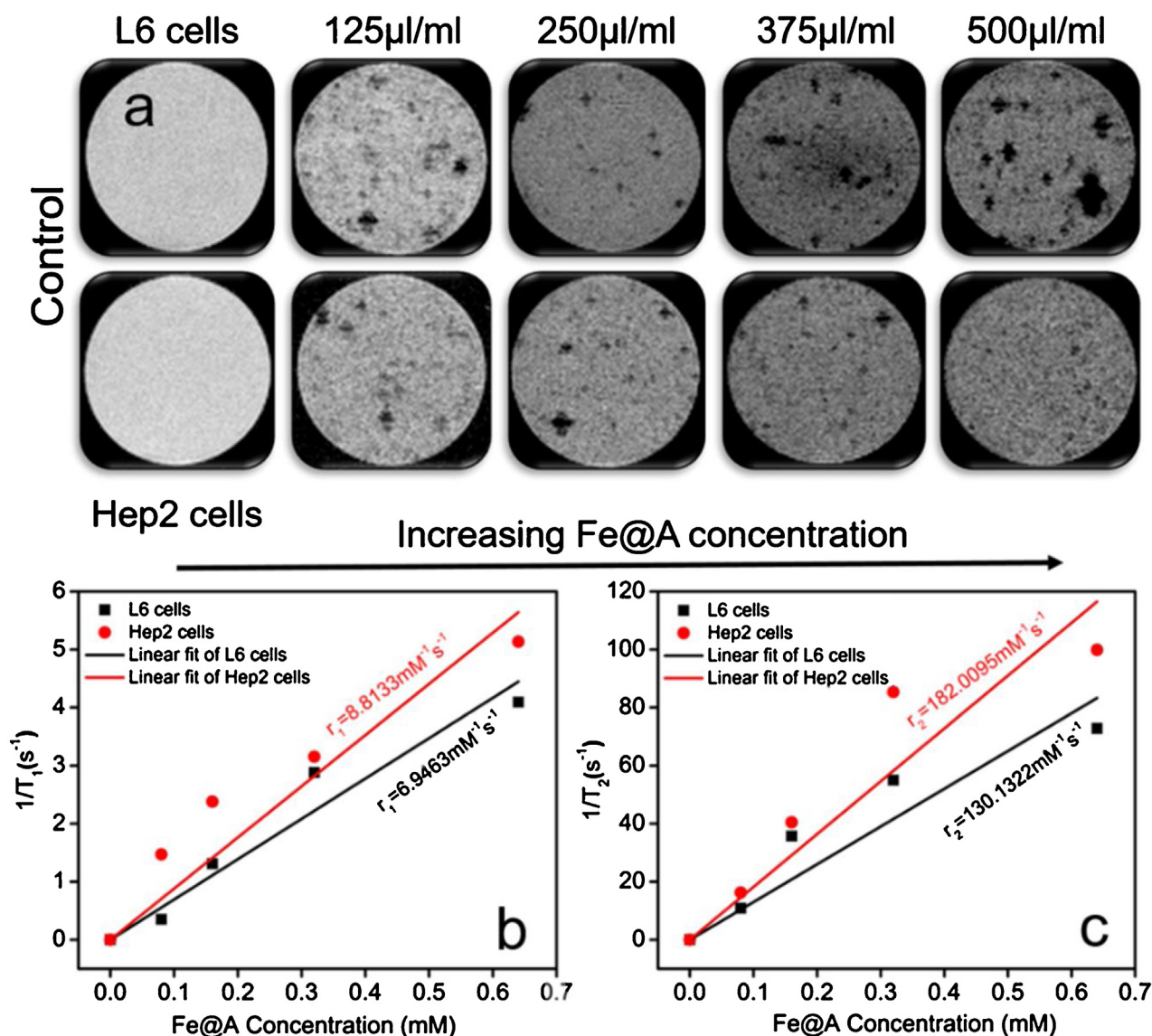


**Fig. 13.** (a) T<sub>2</sub> contrast image of Fe@A as the concentrations increases the darkening also increases, (b) r<sub>1</sub> relaxivity of Fe@A incubated with L6 and Hep2 cells, (c) r<sub>2</sub> relaxivity values of Fe@A incubated with L6 and Hep2 cells.

perturbation of the relaxation processes of the protons in the surrounding water molecules (Pooley, 2005). This causes shortening of the spin-spin relaxation time (T<sub>2</sub>) of the proton, thus resulting in the darkening of the MR images. Such particles even after gold coating, do not lose their characteristics and exhibit T<sub>2</sub> contrast image, which is evident in Fig. 13a. As the concentration is increasing, the NPs show increased darkening of the images in both L6 and Hep2 cell lines as compared to the controls. Moreover, the relaxivity measurements showed r<sub>2</sub> higher than r<sub>1</sub> for both L6 and Hep2 (Table S2 in the ESI). The r<sub>1</sub> and r<sub>2</sub> values for L6 and Hep2 were represented in Fig. 13b & c. The r<sub>2</sub> values are 130.13 mM<sup>-1</sup> s<sup>-1</sup> and 182 mM<sup>-1</sup> s<sup>-1</sup> respectively, while r<sub>1</sub> values were 6.94 mM<sup>-1</sup> s<sup>-1</sup> and 8.81 mM<sup>-1</sup> s<sup>-1</sup> respectively. The enhanced r<sub>2</sub> values confirmed that these NPs are an efficient T<sub>2</sub> contrast agents.

### 3.9.3. Hyperthermal studies of Fe@A at 2.45 GHz

In general, when the MNPs core diameter is less than 20 nm it behaves as a single domain and exhibit superparamagnetism nature (Cullity and Graham, 2008; Krishnan, 2010). These characteristics of NPs generates heating effect under alternating magnetic field (AMF) due to

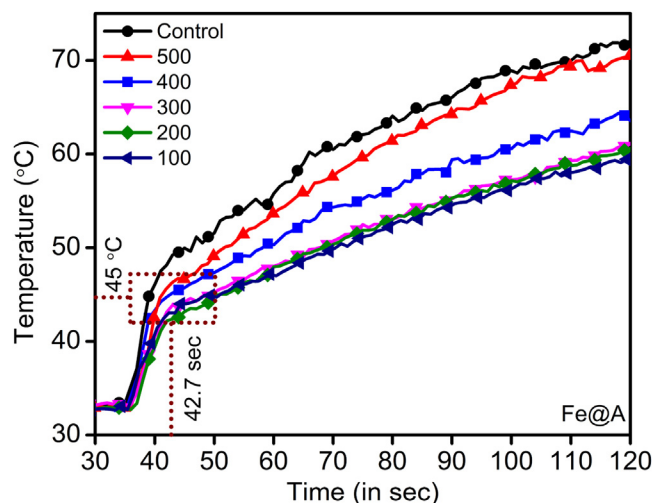


**Fig. 14.** Plot showing increment of temperature as a function of time with the increased conc. of Fe@A.

- Brownian relaxation and/or
- Néel relaxation (Néel, 1950).

Therefore, the hyperthermic performance of **Fe@A CSNPs** at different concentrations (100–500  $\mu\text{g/ml}$ ) were scientifically studied under microwave (MW) at 2.45 GHz for a time span of 120 s at 6 W.

To conduct this studies, the **CSNPs** were suspended in an agar phantom and surrounded by a muscle equivalent phantom. The coaxial antenna was introduced at the agar phantom sphere center along with a temperature sensor and MW was irradiated. From the result it is inferred that the temperature to induce apoptosis in cancer cells (44–45 °C) (Bettaieb and Averill-Bates, 2008) was produced in around 42.7 s and temperature responsible for causing necrosis (45–50 °C) (Meenach et al., 2010) was reached within 45–48 s which is shown in (Fig. 14). We believe that the rapid increment of temperature within a short span of time was purely dependent on the **GNPs** shell onto **Fe** core by retaining the superparamagnetic integrity of core intact within the gold shell. The temperature produced by **Fe@A CSNPs** are much higher when compared to **MNPs** containing ferrofluid with a concentration of 8.8 mg/ml for 5 min at 10 W (García-Jimeno et al., 2012).

#### 4. Conclusion

In summary, we have designed a synthetic route to obtain a gold coated magnetite core@shell (**Fe@A**) nanoparticles using seed-mediated technique along with functional linkers such as **Fa** and **Dox** (**Dox-Fa-Fe@A**). The bimetallic nature of the **CSNPs** was demonstrated using HRTEM and line-mapping techniques. The amalgamation of **Fe** core and the gold shell coating works in a collaborative approach by providing both magnetic properties and biocompatibility. The gold coating not only offers enough protection to **Fe** from oxidation and also the possibility of surface functionalizations.

Therefore, exploiting the core property and the surface capping we have employed it for 3 assorted applications. We inferred that the drug loading efficiency was 94.93% with the cumulative **Dox** release is around 74.73% at pH 5.4 due to acidic environment which simulated the cancer cell endosomal pH. And from the fitting, we found it pursued a first order rate kinetics with high  $R^2=0.9755$  values. As these **CSNPs** were superparamagnetic, in MR imaging it expressed high  $r_2$  values especially with Hep2 cells ( $182 \text{ mM}^{-1} \text{ s}^{-1}$ ) due to **Fa** targeting and confirmed to be  $T_2$  weighted contrast agents. Finally, under MW based hyperthermia, **CSNPs** produced suitable therapeutic temperature which is necessary to induce both apoptosis (42.7 s) and necrosis (45–48 s) rapidly with less concentrations. We confirm that the above versatile applications is solely on the multiple coating of gold layer by maintaining the core property and also providing enough platform for the surface functionalizations. From the above results, currently the **CSNPs** are further studied *in-vivo* in our laboratory.

#### Acknowledgements

This work was supported by CONACyT project 168577. The authors would like to thank Rafael Lara-Estrada for MRI and relaxivity measurements, Carlos Vazquez Calzada for performing confocal microscopy, Norma Barragan Andrade for carrying out cellular experiments, Dr. Francisco Garcia-Sierra for interpreting cellular experiments studies, Dr. Marco A. Garza-Navarro for SQUID analysis and Dr. Victor-Ishrayelu Merupo for helping out in making Fig. 1. We greatly thank Dr. Sergio Armando Tomas for XPS, Jaime E Lara & J. H. Zepeda Peralta for hyperthermia technique, Marcela Guerrero for XRD analysis & FTIR spectroscopy measurements,

Alvaro Angeles Pascual from LANE, for HRTEM and related techniques.

#### Appendix A. Supplementary data

Supplementary data associated with this article can be found, in the online version, at <http://dx.doi.org/10.1016/j.ijpharm.2017.03.071>.

#### References

- Alexiou, C., Arnold, W., Klein, R.J., Parak, F.G., Hulin, P., Bergemann, C., Erhardt, W., Wagenpfeil, S., Lubbe, A.S., 2000. Locoregional cancer treatment with magnetic drug targeting. *Cancer Res.* 60, 6641–6648.
- Angelakeris, M., 2017. Magnetic nanoparticles: a multifunctional vehicle for modern theranostics. *Biochim. Biophys. Acta-Gen. Subj.* 17, 30076–30084.
- Aslan, K., Lakowicz, J.R., Geddes, C.D., 2005. Plasmon light scattering in biology and medicine: new sensing approaches, visions and perspectives. *Curr. Opin. Chem. Biol.* 9, 538–544.
- Barr, T.L., 1978. An ESCA study of the termination of the passivation of elemental metals. *J. Phys. Chem.* 82, 1801–1810.
- Basavegowda, N., Idhayadhulla, A., Lee, Y.R., 2014. Phyto-synthesis of gold nanoparticles using fruit extract of *Hovenia dulcis* and their biological activities. *Ind. Crops Prod.* 52, 745–751.
- Bettaieb, A., Averill-Bates, D.A., 2008. Thermotolerance induced at a fever temperature of 40 degrees C protects cells against hyperthermia-induced apoptosis mediated by death receptor signalling. *Biochem. Cell Biol.* 86, 521–538.
- Cezar, G.G., Quam, J.A., Smith, A.M., Rosa, G.J.M., Piekarczyk, M.S., Brown, J.F., Gage, F.H., Muotri, A.R., 2007. Identification of small molecules from human embryonic stem cells using metabolomics. *Stem Cells Dev.* 16, 869–882.
- Cheng, F.Y., Su, C.H., Yang, Y.S., Yeh, C.S., Tsai, C.Y., Wu, C.L., Wu, M.T., Shieh, D. Bin, 2005. Characterization of aqueous dispersions of  $\text{Fe}_3\text{O}_4$  nanoparticles and their biomedical applications. *Biomaterials* 26, 729–738.
- Cirstoiu-Hapca, A., Bossy-Nobs, L., Buchegger, F., Gurny, R., Delie, F., 2007. Differential tumor cell targeting of anti-HER2 (Herceptin<sup>®</sup>) and anti-CD20 (Mabthera<sup>®</sup>) coupled nanoparticles. *Int. J. Pharm.* 331, 190–196.
- Cullity, B.D., Graham, C.D., 2008. Introduction to magnetic materials. *Clim. Chang.* 2013 – *Phys. Sci. Basis* 53, 1–30.
- Dántola, M.L., Denofrio, M.P., Zurbano, B., Gimenez, C.S., Ogilby, P.R., Lorente, C., Thomas, A.H., 2010. Mechanism of photooxidation of folic acid sensitized by unconjugated pterins. *Photochem. Photobiol. Sci.* 9, 1604–1612.
- Das, M., Mishra, D., Maiti, T.K., Basak, A., Pramanik, P., 2008. Bio-functionalization of magnetite nanoparticles using an aminophosphonic acid coupling agent: new, ultradispersed, iron-oxide folate nanoconjugates for cancer-specific targeting. *Nanotechnology* 19, 415101.
- Dijk, M.A., van Tchebotareva, A.L., Orrit, M., Lippitz, M., Berciaud, S., Lasne, D., Cognet, L., Lounis, B., 2006. Absorption and scattering microscopy of single metal nanoparticles. *Phys. Chem. Chem. Phys.* 8, 3486–3495.
- Ede, S.R., Nithiyantham, U., Kundu, S., 2014. Enhanced catalytic and SERS activities of CTAB stabilized interconnected osmium nanoclusters. *Phys. Chem. Chem. Phys.* 16, 22723–22734.
- El-Hammadi, M.M., Delgado Angel, V., Melguizo, C., Prados, J.C., Arias, J.L., 2017. Folic acid-decorated and PEGylated PLGA nanoparticles for improving the antitumor activity of 5-fluorouracil. *Int. J. Pharm.* 516, 61–70.
- Estrella, V., Chen, T., Lloyd, M., Wojtkowiak, J., Cornnell, H.H., Ibrahim-Hashim, A., Bailey, K., Balagurunathan, Y., Rothberg, J.M., Sloane, B.F., Johnson, J., Gatenby, R.A., Gillies, R.J., 2013. Acidity generated by the tumor microenvironment drives local invasion. *Cancer Res.* 73, 1524–1535.
- Fan, A., Lau, C., Lu, J., 2005. Magnetic bead-based chemiluminescent metal immunoassay with a colloidal gold label. *Anal. Chem.* 77, 3238–3242.
- Gabizon, A., Horowitz, A.T., Goren, D., Tzemach, D., Mandelbaum-Shavit, F., Qazen, M.M., Zalipsky, S., 1999. Targeting folate receptor with folate linked to extremities of poly(ethylene glycol)-grafted liposomes. *In vitro Stud. Bioconjugate Chem.* 10, 289–298.
- García-Jimeno, S., Ortega-Palacios, R., Cepeda-Rubio, M.F.J., Vera, A., Leija, L., Estelrich, J., 2012. Improved thermal ablation efficacy using magnetic nanoparticles: a study in tumor phantoms. *Prog. Electromagn. Res.* 128, 229–248.
- Glangchai, L.C., Calderera-Moore, M., Shi, L., Roy, K., 2008. Nanoimprint lithography based fabrication of shape-specific, enzymatically-triggered smart nanoparticles. *J. Control. Release* 125, 263–272.
- Goon, I.Y., Lai, L.M.H., Lim, M., Munroe, P., Gooding, J.J., Amal, R., 2009. Fabrication and dispersion of gold-shell-protected magnetite nanoparticles: systematic control using polyethyleneimine. *Chem. Mater.* 21, 673–681.
- Guo, M., Que, C., Wang, C., Liu, X., Yan, H., Liu, K., 2011. Multifunctional superparamagnetic nanocarriers with folate-mediated and pH-responsive targeting properties for anticancer drug delivery. *Biomaterials* 32, 185–194.
- Habib, A.H., Ondeck, C.L., Chaudhary, P., Bockstaller, M.R., McHenry, M.E., 2008. Evaluation of iron-cobalt/ferite core-shell nanoparticles for cancer chemotherapy. *J. Appl. Phys.* 103, 07A307.
- Hergt, R., Dutz, S., 2007. Magnetic particle hyperthermia-biophysical limitations of a visionary tumour therapy. *J. Magn. Magn. Mater.* 311, 187–192.

- Hijaz, M., Das, S., Mert, I., Gupta, A., Al-Wahab, Z., Tebbe, C., Dar, S., Chhina, J., Giri, S., Munkarah, A., Seal, S., Rattan, R., 2016. Folic acid tagged nanoceria as a novel therapeutic agent in ovarian cancer. *BMC Cancer* 16, 220.
- Honary, S., Barabadi, H., Gharaei-Fathabad, E., Naghibi, F., 2013. Green synthesis of silver nanoparticles induced by the fungus *penicillium citrinum*. *Trop. J. Pharm. Res.* 12, 7–11.
- Huang, C., Jiang, J., Muangphat, C., Sun, X., Hao, Y., 2011. Trapping iron oxide into hollow gold nanoparticles. *Nanoscale Res. Lett.* 6, 1–5.
- Huang, J., Su, P., Zhao, B., Yang, Y., 2015. Facile one-pot synthesis of  $\beta$ -cyclodextrin-polymer-modified  $\text{Fe}_3\text{O}_4$  microspheres for stereoselective absorption of amino acid compounds. *Anal. Methods* 7, 2754–2761.
- Hui, L., Jiang, E.Y., Zheng, R.K., Bai, H.L., 2004. Structure and magnetic properties of polycrystalline  $\text{Fe}_3\text{O}_4$  films deposited by reactive sputtering at room temperature. *Phys. Status Solidi A* 201, 739–744.
- Chen, X., Tang, Y., Cai, B., Fan, H., 2014. One-pot synthesis of multifunctional GSH-CdTe quantum dots for targeted drug delivery. *Nanotechnology* 25, 235101.
- Jaramillo, T.F., Baecck, S.H., Cuenya, B.R., McFarland, E.W., 2003. Catalytic activity of supported Au nanoparticles deposited from block copolymer micelles. *J. Am. Chem. Soc.* 125, 7148–7149.
- Jin, H., Pi, J., Yang, F., Jiang, J., Wang, X., Bai, H., Shao, M., Huang, L., Zhu, H., Yang, P., Li, L., Li, T., Cai, J., Chen, Z.W., 2016. Folate-chitosan nanoparticles loaded with ursolic acid confer anti-breast cancer activities in vitro and in vivo. *Sci. Rep.* 6, 30782.
- Kamen, B.A., Capdevila, A., 1986. Receptor-mediated folate accumulation is regulated by the cellular folate content. *Proc. Natl. Acad. Sci. U. S. A.* 83, 5983–5987.
- Karaagac, O., Kocak, H., Beyaz, S., Tanrisever, T., 2010. A simple way to synthesize superparamagnetic iron oxide nanoparticles in air atmosphere: iron ion concentration effect. *IEEE Trans. Magn.* 46, 3978–3983.
- Krishnan, K.M., 2010. Biomedical nanomagnetism: a spin through possibilities in imaging, diagnostics, and therapy. *IEEE Trans. Magn.* 46, 2523–2558.
- Lübbe, A.S., Bergemann, C., Riess, H., Schriever, F., Reichardt, P., Possinger, K., Matthias, M., Dörken, B., Herrmann, F., Gürtler, R., Hohenberger, P., Haas, N., Sohr, R., Sander, B., Lemke, A.J., Ohlendorf, D., Huhnt, W., Huhn, D., 1996. Clinical experiences with magnetic drug targeting: a phase I study with 4'-epidoxorubicin in 14 patients with advanced solid tumors. *Cancer Res.* 56, 4686–4693.
- Leamon, C.P., Low, P.S., 1991. Delivery of macromolecules into living cells: a method that exploits folate receptor endocytosis. *Proc. Natl. Acad. Sci. U. S. A.* 88, 5572–5576.
- Leuschner, C., Kumar, C.S.S.R., Hansel, W., Soboyejo, W., Zhou, J., Hormes, J., 2006. LHRH-conjugated magnetic iron oxide nanoparticles for detection of breast cancer metastases. *Breast Cancer Res. Treat.* 99, 163–176.
- Licciardi, M., Scialabba, C., Fiorica, C., Cavallaro, G., Cassata, G., Giammona, G., 2013. Polymeric nanocarriers for magnetic targeted drug delivery Preparation, characterization, and in vitro and in vivo evaluation. *Mol. Pharm.* 10, 4397–4407.
- Lo, C.K., Xiao, D., Choi, M.M.F., 2007. Homocysteine-protected gold-coated magnetic nanoparticles: synthesis and characterisation. *J. Mater. Chem.* 17, 2418.
- Low, P.S., Antony, A.C., 2004. Folate receptor-targeted drugs for cancer and inflammatory diseases. *Adv. Drug Deliv. Rev.* 56, 1055–1058.
- Lu, Y., Low, P.S., 2012. Folate-mediated delivery of macromolecular anticancer therapeutic agents. *Adv. Drug Deliv. Rev.* 64, 342–352.
- Luzar, A., Chandler, D., 1993. Structure and hydrogen bond dynamics of water-dimethyl sulfoxide mixtures by computer simulations. *J. Chem. Phys.* 98, 8160–8173.
- Maeda, H., Wu, J., Sawa, T., Matsumura, Y., Hori, K., 2000. Tumor vascular permeability and the EPR effect in macromolecular therapeutics: a review. *J. Control. Release* 65, 271–284.
- Meenach, S.A., Hilt, J.Z., Anderson, K.W., 2010. Poly(ethylene glycol)-based magnetic hydrogel nanocomposites for hyperthermia cancer therapy. *Acta Biomater.* 6, 1039–1046.
- Mohapatra, S., Pramanik, P., 2009. Synthesis and stability of functionalized iron oxide nanoparticles using organophosphorus coupling agents. *Colloids Surf. A Physicochem. Eng. Asp.* 339, 35–42.
- Moses, M.A., Brem, H., Langer, R., 2003. Advancing the field of drug delivery: taking aim at cancer. *Cancer Cell* 4, 337–341.
- Murphy, C.J., Thompson, L.B., Alkilany, A.M., Sisco, P.N., Boulos, S.P., Sivapalan, S.T., Yang, J.A., Chernak, D.J., Huang, J., 2010. The many faces of gold nanorods. *J. Phys. Chem. Lett.* 1, 2867–2875.
- Néel, L., 1950. Théorie du traînage magnétique des substances massives dans le domaine de Rayleigh. *J. Phys. Radium* 11, 49–61.
- Okahata, Y., Kawase, M., Niikura, K., Ohtake, F., Furusawa, H., Ebara, Y., 1998. Kinetic measurements of DNA hybridization on an oligonucleotide-immobilized 27-MHz quartz crystal microbalance. *Anal. Chem.* 70, 1288–1296.
- Pandey, S., Oza, G., Mewada, A., Shah, R., Thakur, M., Sharon, M., 2013a. Folic acid mediated synaphic delivery of doxorubicin using biogenic gold nanoparticles anchored to biological linkers. *J. Mater. Chem. B* 1, 1361.
- Pandey, S., Thakur, M., Mewada, A., Anjarlekar, D., Mishra, N., Sharon, M., 2013b. Carbon dots functionalized gold nanorod mediated delivery of doxorubicin: tri-functional nano-worms for drug delivery, photothermal therapy and bioimaging. *J. Mater. Chem. B* 1, 4972–4982.
- Peterson, A.W., Wolf, L.K., Georgiadis, R.M., 2002. Hybridization of mismatched or partially matched DNA at surfaces. *J. Am. Chem. Soc.* 124, 14601–14607.
- Pooley, R.A., 2005. Fundamental physics of MR imaging. *RadioGraphics* 25, 1087–1099.
- Říhová, B., 1998. Receptor-mediated targeted drug or toxin delivery. *Adv. Drug Deliv. Rev.* 29, 273–289.
- Rai, A., Prabhune, A., Perry, C.C., 2010. Antibiotic mediated synthesis of gold nanoparticles with potent antimicrobial activity and their application in antimicrobial coatings. *J. Mater. Chem.* 20, 6789.
- Rana, S., Shetake, N.G., Barick, K.C., Pandey, B.N., Salunke, H.G., Hassan, P. a., 2016. Folic acid conjugated  $\text{Fe}_3\text{O}_4$  magnetic nanoparticles for targeted delivery of doxorubicin. *Dalton Trans.* 45, 17401–17408.
- Rao, C.N.R., Müller, A., Cheetham, A.K., 2007. *Nanomaterials Chemistry: Recent Developments and New Directions*. Nanomaterials Chemistry: Recent Developments and New Directions. Wiley-VCH Verlag GmbH & Co. KGaA, Weinheim, Germany doi:http://dx.doi.org/10.1002/9783527611362.
- Ratner, B., Castner, D., 2009. Electron spectroscopy for chemical analysis. *Surf. Anal. Princ. Technol.* 268, 43–98.
- Ravichandran, M., Oza, G., Velumani, S., Ramirez, J.T., Garcia-sierra, F., Andrade, N.B., Vera, A., Leija, L., Garza-navarro, M.A., 2016. Plasmonic/magnetic multifunctional nanoplatfor for cancer theranostics. *Nat. Publ. Gr.* 6, 1–15.
- Reddy, L.H., Arias, J.L., Nicolas, J., Couvreur, P., 2012. Magnetic nanoparticles Design and characterization, toxicity and biocompatibility, pharmaceutical and biomedical applications. *Chem. Rev.* 112, 5818–5878.
- Rejinoold, N.S., Chennazhi, K.P., Nair, S.V., Tamura, H., Jayakumar, R., 2011. Biodegradable and thermo-sensitive chitosan-g-poly(N-vinylcaprolactam) nanoparticles as a 5-fluorouracil carrier. *Carbohydr. Polym.* 83, 776–786.
- Ricles, L.M., Nam, S.Y., Treviño, E.A., Emelianov, S.Y., Suggs, L.J., 2014. A dual gold nanoparticle system for mesenchymal stem cell tracking. *J. Mater. Chem. B* 2, 8220–8230.
- Robinson, I., Tung, L.D., Maenoso, S., Wälti, C., Thanh, N.T.K., 2010. Synthesis of core-shell coated magnetic nanoparticles and their interaction with thiolated DNA. *Nanoscale* 2, 2624–2630.
- Ross, J.F., Chaudhuri, P.K., Ratnam, M., 1994. Differential regulation of folate receptor isoforms in normal and malignant tissues in vivo and in established cell lines. Physiologic and clinical implications. *Cancer* 73, 2432–2443.
- Rybak, S.L., Murphy, R.F., 1998. Primary cell cultures from murine kidney and heart differ in endosomal pH. *J. Cell Physiol.* 176, 216–222.
- Sadhasivam, S., Savitha, S., Wu, C.J., Lin, F.H., Stobiski, L., 2015. Carbon encapsulated iron oxide nanoparticles surface engineered with polyethylene glycol-folic acid to induce selective hyperthermia in folate over expressed cancer cells. *Int. J. Pharm.* 480, 8–14.
- Sahoo, B., Devi, K.S.P., Sahu, S.K., Nayak, S., Maiti, T.K., Dhara, D., Pramanik, P., 2013. Facile preparation of multifunctional hollow silica nanoparticles and their cancer specific targeting effect. *Biomater. Sci.* 1, 647.
- Sanders, J.P., Gallagher, P.K., 2003. Thermomagnetic evidence of  $(-\text{Fe}_2\text{O}_3)$  as an intermediate in the oxidation of magnetite. *Thermochim. Acta* 406, 241–243.
- Scherzinger, A.L., Hendee, W.R., 1985. Basic principles of magnetic resonance imaging—an update. *West. J. Med.* 143, 782–792.
- Schroder, L., Lowery, T.J., Hilty, C., Wemmer, D.E., Pines, A., 2006. Molecular imaging using a targeted magnetic resonance hyperpolarized biosensor. *Science* 80 (314), 446–449.
- Shenderova, O., Hens, S., McGuire, G., 2010. Seeding slurries based on detonation nanodiamond in DMSO. *Diam. Relat. Mater.* 19, 260–267.
- Sonvico, F., Mornet, S., Vasseur, S., Dubernet, C., Jaillard, D., Degrouard, J., Hoebeke, J., Duguet, E., Colombo, P., Couvreur, P., 2005. Folate-conjugated iron oxide nanoparticles for solid tumor targeting as potential specific magnetic hyperthermia mediators Synthesis, physicochemical characterization, and in vitro experiments. *Bioconjug. Chem.* 16, 1181–1188.
- Stella, B., Arpicco, S., Peracchia, M.T., Desmaële, D., Hoebeke, J., Renoir, M., D'Angelo, J., Cattel, L., Couvreur, P., 2000. Design of folic acid-conjugated nanoparticles for drug targeting. *J. Pharm. Sci.* 89, 1452–1464.
- Su, C., Li, H., Shi, Y., Wang, G., Liu, L., Zhao, L., Su, R., 2014. Carboxymethyl- $\beta$ -cyclodextrin conjugated nanoparticles facilitate therapy for folate receptor-positive tumor with the mediation of folic acid. *Int. J. Pharm.* 474, 202–211.
- Sun, C., Sze, R., Zhang, M., 2006. Folic acid-PEG conjugated superparamagnetic nanoparticles for targeted cellular uptake and detection by MRI. *J. Biomed. Mater. Res. – Part A* 78, 550–557.
- Swaan, P.W., 1998. Recent advances in intestinal macromolecular drug delivery via receptor-mediated transport pathways. *Pharm. Res.* 15, 826–834.
- Tang, X., Pan, C.Y., 2008. Double hydrophilic block copolymers PEO-b-PGA: Synthesis, application as potential drug carrier and drug release via pH-sensitive linkage. *J. Biomed. Mater. Res. – Part A* 86, 428–438.
- Thanh, N.T.K., Green, L.A.W., 2010. Functionalisation of nanomaterials for biomedical applications. *Nano Today* 5, 213–230.
- Thaxton, C.S., Mirkin, C.A., Nam, J., 2003. Nanoparticle-based bio-bar codes for the ultrasensitive detection of proteins. *Science* 80 (301), 1884–1886.
- Tiller, W.A., 1991. *The Science of Crystallization*. Cambridge University Press, Cambridge doi:http://dx.doi.org/10.1017/CBO9780511623158.
- Tu, W., 2008. *Quantitative Methods and Applications in GIS*, The Professional Geographer. CRC Press doi:http://dx.doi.org/10.1080/00330120802115458.
- Veiseh, O., Gunn, J.W., Kievit, F.M., Sun, C., Fang, C., Lee, J.S.H., Zhang, M., 2009. Inhibition of tumor-cell invasion with chlorotoxin-bound superparamagnetic nanoparticles. *Small* 5, 256–264.
- Vijayendran, R.A., Leckband, D.E., 2001. A quantitative assessment of heterogeneity for surface-immobilized proteins. *Anal. Chem.* 73, 471–480.
- Vogelson, C.T., Keys, A., Edwards, C.L., Barron, A.R., 2003. Molecular coupling layers formed by reactions of epoxy resins with self-assembled carboxylate monolayers grown on the native oxide of aluminium. *J. Mater. Chem.* 13, 291–296.

- Wang, S., Low, P.S., 1998. Folate-mediated targeting of antineoplastic drugs, imaging agents, and nucleic acids to cancer cells. *J. Controlled Release* 53, 39–48.
- Wang, L., Jiang, X., Ji, Y., Bai, R., Zhao, Y., Wu, X., Chen, C., 2013. Surface chemistry of gold nanorods: origin of cell membrane damage and cytotoxicity. *Nanoscale* 5, 8384–8391.
- Weitman, S.D., Lark, R.H., Coney, L.R., Fort, D.W., Frasca, V., Zurawski, V.R., Kamen, B. A., 1992. Distribution of the folate receptor GP38 in normal and malignant cell lines and tissues. *Cancer Res.* 52, 3396–3401.
- Widder, K.J., Senyei, A.E., Scarpelli, D.G., 1978. Magnetic microspheres: a model system for site specific drug delivery in vivo. *Exp. Biol. Med.* 158, 141–146.
- Wilhelm, C., Lavialle, F., Péchoux, C., Tatischeff, I., Gazeau, F., 2008. Intracellular trafficking of magnetic nanoparticles to design multifunctional biovesicles. *Small* 4, 577–582.
- Chen, J., Wang, Y., Ding, X., Huang, Y., Xu, K., 2014. Analytical Methods on hydroxy functional ionic liquid-modified magnetic nanoparticles. *Anal. Methods* 6, 8358–8367.
- Xu, Z., Hou, Y., Sun, S., 2007. Magnetic core/shell Fe<sub>3</sub>O<sub>4</sub>/Au and Fe<sub>3</sub>O<sub>4</sub>/Au/Ag nanoparticles with tunable plasmonic properties. *J. Am. Chem. Soc.* 129, 8698–8699.
- Wang, Y., Wei, X., Zhang, C., Zhang, F., Liang, W., 2010. Nanoparticle delivery strategies to target doxorubicin to tumor cells and reduce side effects. *Ther. Deliv.* 1, 273–287.
- Yigit, M.V., Mazumdar, D., Lu, Y., 2008. MRI detection of thrombin with aptamer functionalized superparamagnetic iron oxide nanoparticles. *Bioconjug. Chem.* 19, 412–417.
- Wang, Y., Wang, Y., Xiang, J., Yao, K., 2010. Target-specific cellular uptake of taxol-loaded heparin-PEG-folate nanoparticles. *Biomacromolecules* 11, 3531–3538.
- Yu, F., Yao, D., Knoll, W., 2004. Oligonucleotide hybridization studied by a surface plasmon diffraction sensor (SPDS). *Nucleic Acids Res.* 32, e75.
- Yuan, Q., Hein, S., Misra, R.D.K., 2010. New generation of chitosan-encapsulated ZnO quantum dots loaded with drug synthesis, characterization and in vitro drug delivery response. *Acta Biomater.* 6, 2732–2739.
- Zarrin, A., Sadighian, S., Rostamizadeh, K., Firuzi, O., Hamidi, M., Mohammadi-Samani, S., Miri, R., 2016. Design, preparation, and in vitro characterization of a trimodally-targeted nanomagnetic onco-theranostic system for cancer diagnosis and therapy. *Int. J. Pharm.* 500, 62–76.
- Zhang, J., Rana, S., Srivastava, R.S., Misra, R.D.K., 2008. On the chemical synthesis and drug delivery response of folate receptor-activated: polyethylene glycol-functionalized magnetite nanoparticles. *Acta Biomater.* 4, 40–48.
- Zhang, W., Patel, K., Schexnider, A., Banu, S., Radadia, A.D., 2014. Nanostructuring of biosensing electrodes with nanodiamonds for antibody immobilization. *ACS Nano* 8, 1419–1428.
- Zhang, L., Zhu, D., Dong, X., Sun, H., Song, C., Wang, C., Kong, D., 2015. Folate-modified lipid-polymer hybrid nanoparticles for targeted paclitaxel delivery. *Int. J. Nanomed.* 10, 2101–2114.